Internal derangements of joints-past, present, and future

Sutter, Reto ; Stoel, Berend C ; Buck, Florian M ; Andreisek, Gustav ; Morelli, John N ; Hodler, Jürg ; Li, Xiaoming ; Pfirrmann, Christian W A

Abstract: The past 50 years have transformed imaging of the joints. Whereas musculoskeletal imaging consisted predominantly of conventional radiography when Investigative Radiology was founded as a journal, the arrival of new imaging modalities, and above all, the introduction of magnetic resonance imaging, resulted in a paradigm shift: In addition to visualizing osseous structures, now the detailed depiction of soft tissue structures became part of routine clinical imaging and had a major impact on understanding pathophysiology and patient treatment. This article analyzes the patterns of innovation that were essential for the transformation of musculoskeletal radiology. Furthermore, state-of- the-art joint imaging is described through 9 key concepts, including both cutting-edge clinical applications as well as topics at the forefront of musculoskeletal research. Eventually, emerging trends are outlined that will likely shape musculoskeletal radiology in the next decades.

DOI: https://doi.org/10.1097/RLI.0000000000000162

Internal Derangements of Joints—Past, Present, and Future

Reto Sutter, MD,† Berend C. Stoel, PhD,‡ Florian M. Buck, MD,*† Gustav Andreisek, MD, MBA,†§ John N. Morelli, MD,|| Jürg Hodler, MD, MBA,†§ Xiaoming Li, MD, PhD,¶ and Christian W.A. Pfirrmann, MD, MBA*†*

Abstract: The past 50 years have transformed imaging of the joints. Whereas musculoskeletal imaging consisted predominantly of conventional radiography when *Investigative Radiology* was founded as a journal, the arrival of new imaging modalities, and above all, the introduction of magnetic resonance imaging, resulted in a paradigm shift: In addition to visualizing osseous structures, now the detailed depiction of soft tissue structures became part of routine clinical imaging and had a major impact on understanding pathophysiology and patient treatment. This article analyzes the patterns of innovation that were essential for the transformation of musculoskeletal radiology. Furthermore, state-of- the-art joint imaging is described through 9 key concepts, including both cutting-edge clinical applications as well as topics at the forefront of musculoskeletal research. Eventually, emerging trends are outlined that will likely shape musculoskeletal radiology in the next decades.

Key Words: musculoskeletal imaging, MSK, radiography, CT, MRI, history, articular, joint, trends

(*Invest Radiol* 2015;00: 00–00)

Like many subspecialties of radiology, musculoskeletal (MSK) imaging has undergone a major transformation in the past 50 years. This is especially apparent in imaging of the joints. Whereas in 1965, the radiological diagnosis was mainly focused on the osseous parts of the joints, we are now able to depict cartilage, soft tissues, nerves, and even joint inflammation directly. With the widespread use of surgical techniques such as arthroscopic surgery, MSK imaging is gaining an ever more crucial role in assessing the joints for obtaining a diagnosis as well as for therapy planning.

In the following section of this review, we analyze the patterns of innovation that were essential for the transformation of MSK imaging in the past 50 years. Important contributions for this chapter are based on interviews with several distinguished leaders in the field of MSK, including Michael Recht, Mini Pathria, Jürg Hodler, Thomas Böni, and Siegfried Trattnig.

We will proceed to the description of the state-of-the-art joint imaging as exemplified through 9 key concepts, a discussion that will include both cutting-edge clinical applications as well as topics at the forefront of research. Experts in the field have contributed to these individual key concepts.

The final section is dedicated to the future of MSK imaging. Whereas none of the authors is clairvoyant, we will nevertheless try to attempt some of the trends that will shape MSK radiology in the coming decades.

Received for publication February 28, 2015; and accepted for publication, after revision, March 17, 2015.

From the *Department of Radiology, Orthopedic University Hospital Balgrist; †Faculty of Medicine, University of Zurich, Zurich, Switzerland; ‡Department of Radiology, Division of Image Processing, Leiden University Medical Center, Leiden, the Netherlands; §Department of Radiology, University Hospital Zurich, Zurich, Switzerland; ||Department of Radiology, St. John's Medical Center, Tulsa, OK; and ¶Department of Radiology, Tongji Hospital, Tongji Medical College, Huazhong University of Science and Technology, Wuhan, China.

The authors report no conflicts of interest.

Reprints: Reto Sutter, MD, Department of Radiology, Orthopedic University Hospital Balgrist, Forchstrasse 340, 8008 Zurich, Switzerland. E-mail: reto.sutter@balgrist.ch.

ISSN: 0020-9996/15/0000–0000

PATTERNS OF INNOVATIONS

The past 50 years have transformed imaging of the joints, as demonstrated by the variety of MSK papers that appeared in *Investigative Radiology* over this period. What were the big leaps that shaped the way we image the joints today? Let us take a look at some of the patterns of innovation, beginning with the transformations in conventional radiography.

Radiographs remain essential for imaging of the joints for evaluation of diseases such as osteoarthritis (OA), inflammatory arthritis, and for evaluation of trauma. Fifty years ago, MSK imaging consisted predominantly of conventional radiography.[1,2] In special cases, radiograph-based modalities such as fluoroscopy, arthrography, and angiography were performed.[3–5] Most questions in MSK imaging addressed bone pathology, and this field of radiology was appropriately termed osteoradiology.[6]

In this state of joint imaging in the 1960s and 1970s, many soft tissue diagnoses, such as ligament or meniscal tears, were often overlooked, since the adjacent osseous structures revealed no abnormality. As a result, patients had to undergo invasive diagnostic arthrotomy or arthroscopy to obtain a diagnosis. Radiographs have come a long way and remain the basis for many aspects of MSK imaging. The introduction of digital radiography allowed both for significant improvement in image quality and substantial reduction in radiation dose.[7]

The advent of computed tomography (CT) marked a shift in clinical radiology from projection radiography and conventional x-ray tomography to cross-sectional imaging. This is specifically evident in imaging of bone tumors and in the evaluation of fractures.[8]

Initially, CT acquisition times were long, and only 2-dimensional (2D) data were available for routine clinical imaging. Whereas cross-sectional anatomical depictions of the joints and anatomic measurements were possible,[9,10] it was the establishment of secondary multiplanar reconstructions based on a 3D data set that transformed the use of CT in MSK imaging.[11,12]

Three-dimensional images for MSK imaging were initially generated from 2D CT data, with considerable loss of information depending on the orientation of the original images, limiting the role of CT in the early days.[13] With the advent of spiral CT and later multislice CT, this changed dramatically. It then became possible to generate secondary reconstructions based on a 3D data set, with detailed depiction of the osseous anatomy on multiplanar imaging,[14] allowing an accurate diagnosis as well as improved surgical planning.

Computed tomography arthrography was also subsequently introduced, representing a major advance over fluoroscopic arthrography, allowing depiction of the articular cartilage with high resolution, and enabling the indirect depiction of soft tissue pathology such as rotator cuff tears.[15,16]

The success story of MSK imaging over the past 50 years is closely linked to the development and the success of magnetic resonance imaging (MRI). The first-ever human MRI image was produced by Sir Peter Mansfield in 1977 and was actually an MSK image, as it was a cross section of the finger of Dr. Andrew Maudsley.[17] For clinical imaging, it soon became clear that the introduction of MRI was a real paradigm shift[18]: In addition to visualizing osseous structures, MRI allowed detailed depiction of soft tissue structures such as muscles, ligaments, menisci, and articular cartilage.[19–24] Over time, the availability

of high-resolution joint MRI in routine clinical practice nearly eliminated the need for diagnostic arthroscopy. Development of MR arthrography had a major impact on treatment decisions particularly for hip and shoulder imaging,[25–27] with evaluation of cartilage and labrum integrity, but also depiction of rotator cuff tears and the associated muscle atrophy in the shoulder.[28,29]

Our understanding of pathophysiology has been altered substantially by the availability of high-resolution MRI. Whereas macroscopic anatomy taught us how different parts of the joints are shaped, at MRI, an abundance of anatomical variants and seemingly pathological findings are visible.[30,31] For the clinical use of MSK MRI, it became essential to distinguish real pathology from variants and from early degeneration that have no or limited clinical impact, a distinction that has proven to be challenging in specific cases up to the present time. This is exemplified by the diagnosis of meniscal tears. Whereas menisci are homogenously hypointense on the standard MRI sequences in young individuals, a variety of signal changes are visible at MRI of the knee in most middle-aged and elderly patients.[32] Several studies have shown that not all meniscal tears are linked to trauma or symptoms and have influenced the reporting of abnormal findings.[33,34]

Another area where high-resolution MRI has enhanced our understanding of pathophysiology is the hip joint. Femoroacetabular impingement (FAI) was not known 50 years ago and has only been recognized in the past 15 years as the major cause of early-onset OA in nondysplastic hips.[35] A combination of clinical observations, biomechanical considerations, and imaging findings have been crucial in developing and consolidating the concept of FAI, with MRI widely used today in the evaluation of patients with suspected FAI. However, MRI has also been used to demonstrate that substantial variability of the osseous anatomy is present at the proximal femur in healthy individuals and to prove that some of these findings should not be considered abnormal, therefore aiding in the prevention of FAI overdiagnosis.[36]

In the 1980s, the acquisition of MR images was a lengthy process of approximately 1 hour, and the resultant images were only low resolution. In the subsequent decades, multiple important innovations in MR hardware resulted in increased field strength and gradient strength, whereas substantial improvements in coil design, including the introduction of multichannel receiving coils, combined to dramatically change both acquisition times and image quality.[37,38] These advances in technical innovations are described in detail in an excellent review by Ai et al.[39] Furthermore, the development of advanced pulse sequences such as fast spin echo sequences, parallel imaging, short echo–time MRI, and MRI spectroscopy truly revolutionized MSK radiology.[39–43]

Technical advances in MSK MRI continue at a rapid pace today with the introduction of pulse sequences that allow for imaging of metal prosthetics[44] and with high-resolution 3D sequences for imaging of articular cartilage.[45] At the cutting edge of research is the investigation of so-called biochemical imaging of cartilage, a technique that aims at detection of early cartilage degeneration before macroscopic cartilage defects are visible on conventional MR sequences.[46–49] Finally, also the introduction of 7-T MRI is expected to bring unprecedented insight into pathophysiology of cartilage disease.[50–52]

Fifty years ago when MSK radiology was mainly based on conventional radiography, few radiologists subspecialized in dedicated MSK imaging. With the arrival of new imaging modalities on the scene, and in particular, after the introduction of MRI in routine clinical imaging, MSK radiology became established as a subspecialty. This development is mirrored in the establishment of specialized MSK societies such as the International Skeletal Society (ISS) in 1972, the European Society of Musculoskeletal Radiology (ESSR) in 1993, as well as many national MSK imaging societies. Furthermore, specialized MSK fellowships were established in the United States in the late 1970s and early 1980s that had a major impact in the spreading of MSK radiology as a subspecialty.[6]

STATE-OF-THE-ART IMAGING OF THE JOINTS—KEY CONCEPTS

Musculoskeletal radiology is a wide field; to give an overview of the state of the art of joint imaging, we present 9 key concepts that either focus on a current technology for clinical application or research.

High-Resolution MRI

High-resolution MRI is imperative for the accurate diagnosis of abnormalities involving the relatively small structures of the joints (Fig. 1). Such examinations must also be performed within a relatively short period of time (15–30 minutes) to maintain adequate patient throughput. The theoretical doubling of signal-to-noise ratio (SNR) at 3.0 T can be used as a type of currency and traded for higher-resolution imaging and/or shorter scan acquisition times. As a result, 3.0-T MSK MRI has been widely adopted for noninvasive evaluation of the MSK system.

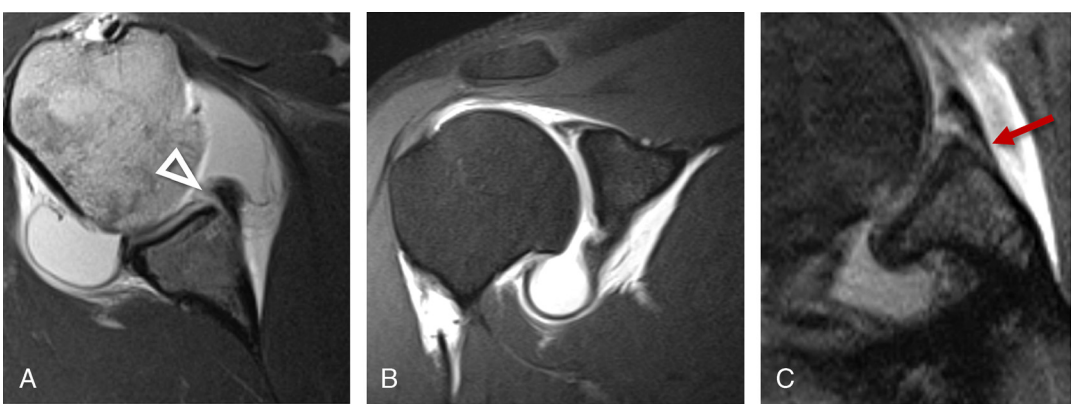

FIGURE 1. High-resolution MR arthrography image of the right shoulder with a T1-weighted axial image (A), a fat-saturated coronal T2-weighted image (B), and an additional fat-saturated T2-weighted image (C) obtained with abduction and external rotation positioning. Images in standard positioning demonstrate an anteroinferior tear of the glenoid labrum (arrowhead in A), consistent with anterior glenohumeral instability. Abduction and external rotation images demonstrate stripping of the periosteum (arrow in C), consistent with a Perthes-type lesion. The images were obtained using a high-resolution 0.6 × 0.4 × 0.2-mm 2D TSE protocol after the injection intra-articular contrast at 3 T with a dedicated 16-element shoulder coil and a parallel imaging acceleration factor of 2. Figure 1 can be viewed online in color at www.investigativeradiology.com.

Dedicated coils are essential for optimal image quality in high-resolution MRI regardless of the joint imaged. Improved coil geometry and the greater number of independent coil elements have greatly improved SNR and image quality. However, multielement coils can also be aligned in the phase-encoding dimension, enabling implementation of parallel imaging.[53] With parallel imaging, the differing spatial sensitivities of each coil element is exploited and used to undersample k-space in the phase-encoding direction. As such, scan time can be accelerated proportional to the degree of undersampling. Each portion of undersampled phase- encoding data is then combined either before (ie, generalized autocalibrating partially parallel acquisition [GRAPPA] or simultaneous acquisition of spatial harmonics [SMASH])[54] or after the Fourier-Transform (ie, sensitivity encoding [SENSE])[55] to produce the final image.

Other recent advances in MR data sampling are poised to further reduce the scan acquisition time for high-resolution MSK MRI. For example, in the knee and shoulder 2D turbo spin echo (TSE) sequences have been primarily used to generate variously weighted sequences in axial, coronal, and sagittal planes. Despite use of moderate echo train lengths and parallel imaging factors of 2, each high-resolution sequence (for example, $0.3 \times 0.3 \times 0.8$ mm) may still require 3 to 4 minutes. One solution to this is use of 3D imaging to obtain isotropic MR images, which can then be reconstructed in arbitrary planes, for example, by using an isotropic 3D sampling perfection with application-optimized contrasts using different flip angle evolutions (SPACE) TSE sequence with intermediate weighting (Fig. 2).[56] In the knee, such images with 6-mm isotropic resolution have been shown to be similar to conventional 2D TSE sequences for characterization of meniscal tears, and superior to 2D techniques for the detection of flap tears.[57,58] Other results in the shoulder have been equally promising: In one study, 3D TSE sequences demonstrated near-perfect concordance with 2D TSE and decreased examination time by almost 40%.[59] Three-dimensional imaging techniques in combination with MR arthrography have also proven to be suitable substitutes for the evaluation of bony Bankart lesions and glenoid bone loss in anterior shoulder instability.[60]

With further increases in parallel imaging acceleration, SNR becomes limited by signal undersampling and g-factor noise amplification, which is dependent on the encoding capabilities of the receiver array. This is typically observed as a loss of signal-to-noise within the center of the image, where coil sensitivity profiles differ least. G-factor noise is also problematic when 2D parallel imaging is used in 3D and simultaneous multislice (SMS) imaging. Ideally, the number and arrangement of coil elements could be optimized for each application, but in reality, hardware limitations and diversity in patient size and weight prevent this. Controlled aliasing in parallel imaging results in higher acceleration CAIPIRINHA is a reconstruction algorithm that modifies aliasing conditions associated with parallel imaging in a controlled manner by cycling the phase of the radiofrequency pulse applied to each slice.[61,62] This controlled aliasing with each slice results in fewer areas, where multiple slices contribute signal to the undersampled image.

As parallel imaging is typically associated with a decreased SNR, a new technique called multiband phase-constrained parallel MRI uses the simultaneous excitation of several slices by means of multiband radiofrequency pulses and then separates the slices using parallel MRI reconstruction algorithms.[63,64] The phase-constrained reconstruction uses background phase variations in addition to coil sensitivity variations to obtain the MRI image with a substantial reduction in scanning times.[63] This may have a major impact on MRI with a dramatic acceleration of imaging at field strengths greater than 3 T, diffusion-weighted imaging (DWI), functional MRI, and other techniques.[65]

Another promising approach for scan time reduction is compressed sensing, a technique that aims to reconstruct images from fewer measurements than originally thought necessary. Most MR images are sparse in various transform domains, and this sparsity can be exploited by randomly undersampling k-space data. This technique is complementary to and can be used alongside other k-space undersampling techniques previously discussed. Whereas initial results are promising, much work remains to be done before this can be transitioned to the clinical routine.[66]

MRI Arthrography of Femoroacetabular Impingement

Direct MRI arthrography of the hip joint plays a major role in diagnosing femoroacetabular impingement (FAI) and planning of surgery by depicting both the osseous abnormalities of FAI and the labrum and cartilage damage associated with FAI.[67] Patients with FAI typically show either osseous overcoverage of the acetabulum (pincer-type FAI), osseous deformities of the femoral head-neck junction (cam-type FAI), or both (mixed-type FAI).[68,69] Although some authors proposed to assess the pincer-type deformity with CT or MRI, it is best assessed with standard pelvic radiographs.[70] For the cam-type deformity, CT or MRI offer a distinct advantage over standard radiographs, since the 3D contour of the femoral head-neck junction can be assessed on radial images around the femoral head.[70] As the maximum cam-type deformity is commonly located at the anterosuperior position, this allows a more accurate assessment. However, there is much debate on how to best assess the cam-type deformities. Initially, Nötzli et al[71] introduced the alpha angle to define a cutoff value for cam-type deformities, but it has been shown that the alpha angle is not a reliable tool

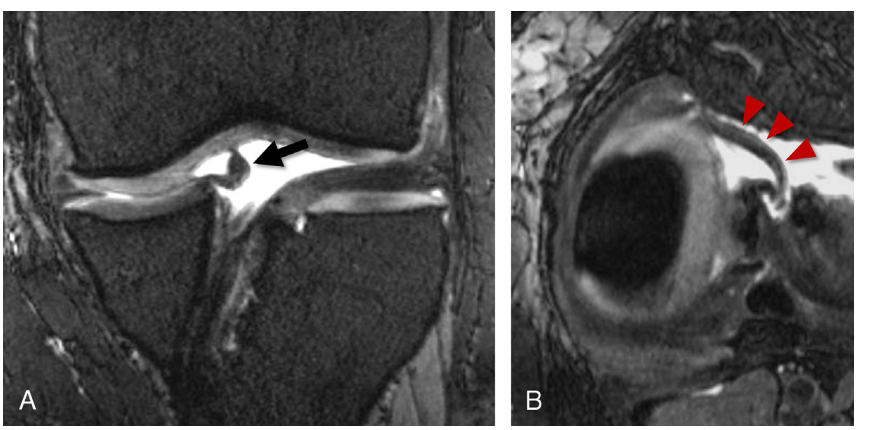

FIGURE 2. Three-dimensional SPACE TSE fat-saturated intermediate-weighted image in the coronal plane (A) with additional axial reconstruction (B) in the plane of the meniscus enabling improved delineation of the anterior root tear (arrow in A and arrowheads in B) in a patient after previous reconstruction of the anterior cruciate ligament. Acquisition was performed with a 0.6-mm isotropic spatial resolution allowing for image reconstruction in both standard and arbitrary planes. Figure 2 can be viewed online in color at www.investigativeradiology.com.

to assess cam-type deformities owing to a large overlap of values between healthy individuals and patients.[36,72] Alternative measurement techniques such as the femoral offset or the femoral distance around the circumference of the femoral head have been proposed, but they do not show a more accurate discrimination between healthy individuals and patients with FAI than the alpha angle.[73]

Other factors have been recognized that may contribute to the development of FAI, either in combination with cam- and pincer-type deformities, or even as an isolated pathology, such as extreme hip motion in young athletes or ballet dancers, and abnormal femoral antetorsion.[74–76]

In patients with suspected FAI, MR arthrography is the standard of care for the evaluation of the labrum and acetabular cartilage, but CT arthrography may be performed as an alternative in patients with contraindications for MR imaging.[77] Several publications have assessed whether MR arthrography can be replaced by noncontrast MRI, with varying sensitivity and specificity; but currently, MRI arthrography is reported to have a higher accuracy compared to noncontrast MRI (Fig. 3).[78,79]

The detection of defects of the articular cartilage is often more difficult than the detection of labral tears, as the cartilage layers are very thin and have a spherical morphology.[80] Most cartilage defects are found at the anterosuperior portion of the acetabulum. Whereas MR arthrography is currently more accurate in detecting small cartilage defects of the acetabulum than noncontrast MRI, both modalities have a similar accuracy for diagnosing cartilage defects of the femoral head and extensive cartilage defects that are equivalent to early-stage OA.[79,81] Currently, several MRI techniques (eg, delayed gadolinium-enhanced MRI of cartilage [dGEMRIC]) are being evaluated to detect early cartilage degeneration of the hip before macroscopic defects are present, to allow for timely and successful treatment of FAI before extensive joint damage is present.[82] Whereas short-term results and the first 10-year follow-up results after FAI surgery are promising, the long-term benefits of surgical treatment of FAI are still under investigation at this time.

Advanced Cartilage Imaging for Detection of Early-Onset OA

Despite the increasing spatial resolution of MRI of the joints, the diagnosis of early-onset OA remains a challenge. We will briefly review some of the cartilage mapping techniques that are being evaluated in the preclinical stage for assessing glycosaminoglycan (GAG) loss and collagen breakdown as typical features of early-onset OA.[83,84]

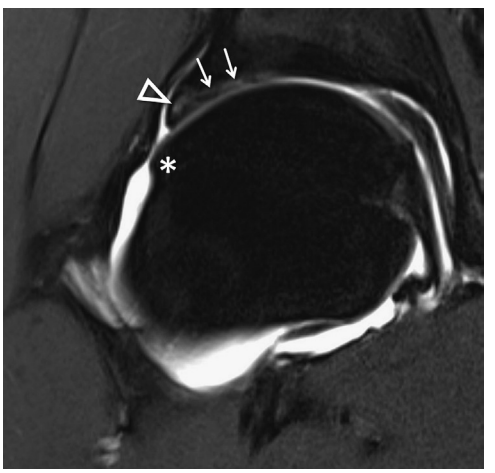

FIGURE 3. Cam-type FAI in a 20-year-old professional male soccer player seen on a coronal intermediate-weighted fat-suppressed MR arthrography of the right hip. When the cam-type deformity (asterisk) at the femoral head-neck junction is rotated into the hip joint during flexion and internal rotation, this leads to labrum and cartilage damage over time, as demonstrated here with a labral tear (arrowhead) and delamination of the adjacent acetabular cartilage (arrows).

T2 mapping uses multiecho spin-echo sequences to assess the collagen microstructure in the extracellular matrix of the cartilage.[85,86] Cartilage T2 values mainly depend on 3 factors: orientation of the collagenous fiber in the cartilage, content of collagenous fiber, and content of water. T2 values decrease progressively from surface layer to deep layer in the normal cartilage because of anisotropy in different layers. Damage to the extracellular matrix is associated with increased T2 relaxation times.[87] Apprich et al[88] used quantitative T2 mapping at 3-T MRI in a study with 43 patients who already had macroscopic cartilage defects to demonstrate that the adjacent cartilage also featured some cartilage degeneration. A study by Mosher et al[89] found that T2 values of the surface layer in the tibiofemoral cartilage decreased after running, so T2 mapping can even supply some information about cartilage reaction to physiologic weight bearing. Regional differences have been described for T2 mapping depending on the orientation of the cartilage tissue relative to the main magnetic field, so standard T2 values can vary according to joint subregions and the placement of the patient in the scanner.[90]

T1rho imaging uses "spin lock" pulses to lock the transverse magnetization and drive the recovery of longitudinal magnetization as a means of estimating proteoglycan change in the joint cartilage that is associated with joint degeneration.[91] With progressive joint degeneration, the T1rho values are increased.[92] In patients with varying degrees of knee OA, significant differences in T1rho values have been documented between subregions of menisci and femorotibial cartilage.[93,94] Furthermore, T1rho seems to be more sensitive for the detection of early cartilage degeneration than T2 mapping.[86]

The dGEMRIC is either with intravenous or direct intra-articular application of contrast.[49] The technique is based on the concentration of negatively charged contrast molecules in an inversely proportional manner to the negatively charged GAGs in degenerated articular cartilage in association with OA.[95,96] The concentration of gadolinium-DTPA^{2-} can be assessed by measuring T1 values, and T1 mapping produces a visual approximation of the GAG distribution to detect areas with proteoglycan deficiency.[84] Recent work by Endo et al[97] further showed the effectiveness of dGEMRIC imaging in histological and biochemical evaluation of repair tissue at early stage after allograft chondrocyte implantation.

In addition to ^{1}H, sodium (^{23}Na) is another element that can be used to aid in cartilage imaging. The proteoglycan sulfate and carboxylate groups of GAG molecules create a fixed negative charge within the cartilage, and the binding of cations (primarily Na^{+}) to those negative charges allows the maintenance of electroneutrality within the extracellular matrix.[98] As the sodium will distribute in proportion to the negative charges of GAG molecules in degenerated articular cartilage, the area of proteoglycan loss caused by cartilage degeneration can be visualized. Recent work showed sufficient sensitivity of sodium MRI to GAG changes in articular cartilage of ankle and subtalar joints.[52] The current limitations of sodium imaging are the requirements of dedicated hardware as well as high-field MRI.

Synovitis Assessment With MRI

Rheumatoid arthritis (RA) is the prototypical inflammatory synovial disease, a chronic inflammatory condition of the joints most commonly involving the joints of the proximal hand. The advent of disease-modifying antirheumatic drugs has rendered the early diagnosis of RA imperative, as early treatment with such therapies has been shown to improve disease outcomes.[99] The high cost of these therapies makes the accuracy of the RA diagnosis even more important. Magnetic resonance imaging detects subtle inflammatory changes in RA before the detectability of erosions by radiography and CT. Magnetic resonance

imaging has thus become an indispensable tool in the evaluation of early inflammatory changes in RA and other rheumatologic conditions.

Magnetic resonance protocols for detection of RA and other inflammatory conditions differ from those used for the detection of orthopedic conditions. In addition to standard TSE sequences including contrast-enhanced sequences, some 3D TSE techniques (ie, SPACE or CUBE) may be used, as they enable reconstructions in any arbitrary plane, and as acquisition of images with thin slices are useful for detecting erosions.

Three MRI findings in RA—bone marrow edema, tenosynovitis, and bone erosions—are included as standard criteria for the assessment of outcomes in the outcome measures in rheumatology clinical trials (OMERACT).[100,101] Bone marrow edema is an early manifestation of RA. This edema is the most important prognostic factor in RA[102] and follows the typical pattern of erosions,[103] suggesting it is a precursor lesion. In one study, RA progression was detected with 82% sensitivity and specificity using an algorithm incorporating MR imaging criteria.[104] Bone marrow edema is also the most specific of the aforementioned signs[105] on noncontrast images with a specificity of approximately 83%. T1-weighted images are most useful for visualization of erosions, which are defined by RAMRI criteria as "a sharply marginated bone lesion with correct juxta-articular localization and typical signal characteristics, which is visible in 2 planes with a cortical break seen in at least one plane."[106] Magnetic resonance imaging is significantly more sensitive than radiography (61% vs 24%) for erosion detection.[107] Synovial inflammation in RA eventually progresses to development of a cellular, inflammatory pannus[108] typically with low signal on T1- and high signal on T2-weighted images. This pannus is responsible for cartilage and bone destruction. Synovial enhancement is assessed with contrast-enhanced MRI. Dynamic contrast-enhanced MRI has been shown to be useful in differentiating active versus inactive RA.[109] If intravenous contrast cannot be given, as in the case of patients with renal failure, diffusion tensor imaging has been described as an alternative,[110] with similar sensitivity in detection versus contrast-enhanced MRI. Anisotropic proton motion detected by this technique within joint fluid suggests the presence of an inflammatory component. Tenosynovitis, as detected with MRI or Sonography, has been shown to be a useful marker for RA as well.[111]

Magnetic resonance imaging is also useful for the differentiation among etiologies of inflammatory arthropathy. Polyarticular psoriatic arthritis may be difficult to distinguish from rheumatoid arthritis (RA) in cases where the distal interphalangeal joints are not involved and laboratory values are equivocal. Periostitis and synovitis are more frequent in the proximal interphalangeal joints in psoriasis, whereas synovitis and erosions in the wrist are more typical in RA.[112] Inflammation in psoriatic arthritis also frequently extends beyond the joint capsule, related to inflammatory enthesopathy. Dynamic contrast-enhanced MRI has been described as a way to distinguish the 2 conditions with synovial enhancement persisting on 15-minute delayed images in RA.[113] Similar to RA, the psoriatic arthritis MRI score has been confirmed to be a reliable way to monitor inflammation in psoriatic arthritis clinical trials.[114]

MRI Metal Artifact Reduction

The number of patients with joint replacement has increased rapidly worldwide, and both hip and knee replacements are overall considered to be very successful treatments for end-stage OA. In patients with residual pain or other complications, it is often challenging to reach the correct diagnosis, as abnormalities of both the bone and the periarticular soft tissues have to be evaluated. After total knee arthroplasty up to 29% of patients have substantial pain at rest or during walking 1 year after surgery, and imaging plays an important part in the evaluation of these patients.[115]

For total hip arthroplasty (THA), the results are generally better than for total knee arthroplasty; but in recent years, it has been recognized that one particular type of implants leads to an increased rate of complications[116]: Metal-on-metal implants showed promising initial results, but many of these products have been recalled owing to a large number of cases with metallosis and various complications often described as “adverse local tissue reaction”.[117] This can result in aggressive soft tissue destruction and pseudotumors—and MRI has proved to be important in the diagnosis of those complications.[118] For a long time, MRI of joint replacement was not possible owing to enormous metal artifacts around the prosthesis that resulted in nondiagnostic images. Since the beginning of this century, however, rapid developments in MRI technology have resulted in a paradigm shift.[119] Initially, MRI was performed in patients with THA to assess the muscles and tendons around the greater trochanter in patients with insufficiency of the hip abductors or with greater trochanteric pain syndrome.[120] In recent years, it has even become possible to evaluate the joint capsule, periarticular ligaments, and the bone around the metal in patients with total hip or knee arthroplasty.[121]

A variety of basic principles can be used to reduce metal artifacts for prosthesis MRI, such as using fast spin-echo sequences instead of gradient-echo sequences, using a small slice thickness, and scanning at 1.5 T rather than at 3 T, since the artifact size is directly proportional to the magnetic field strength. A very powerful but simple technique is to increase the bandwidth during slice selection and during readout to reduce metal artifacts, although this comes at the price of a reduced SNR.[122] As spectral fat saturation typically fails around metal implants, short tau inversion recovery (STIR) sequences are preferred for MRI of joint replacement. Short tau inversion recovery imaging is especially helpful if the bandwidth of the inversion radiofrequency pulse is matched to the increased bandwidth of the excitation radiofrequency pulse, albeit this increases the specific absorption rate during scanning.[123]

Although these basic techniques for metal artifact reduction are easy to implement, they are only able to reduce artifacts in the image plane to a certain degree, leaving the substantial distortions from adjacent image planes untouched. New multispectral sequences allow these through-plane distortions to be addressed, either with a repeated frequency-selective excitation (multiacquisition with variable resonance image combination [MAVRIC] technique), by adding an additional slice-encoding gradient (slice encoding for metal artifact correction [SEMAC] technique), or by combining these 2 techniques (Fig. 4).[44,124] Whereas this results in an improved depiction of the bone-metal interface of the prosthesis, acquisition time is increased substantially.

Sequences with through-plane distortion correction have a substantial clinical impact in patients with THA, with SEMAC enabling the better detection of soft tissue pathologies, such as tears of the abductor tendons, trochanteric bursitis, and synovitis, but also by depicting periprosthetic osteolysis.[125] SEMAC can also be incorporated in the diagnostic algorithm for patients with a painful knee arthroplasty, since it features the same accuracy as CT for detecting periprosthetic osteolysis but also can depict bone marrow edema around the prosthesis or collateral ligament damage in patients with instability.[126]

While MRI of hip and knee replacements has been successfully introduced in routine practice, current acquisition times are quite long, with durations of 6 to 8 minutes for advanced sequences. With further technical improvements such as compressed sensing, it is expected that MRI metal artifact reduction will get both faster and the reduction of residual artifacts even better.[127] Furthermore, metal artifact reduction at 3 T is becoming feasible for clinical application.[128,129]

Helical CT With 3D Modeling and Surgical Planning of Osteotomies

The concept of 3D bone reconstruction based on helical CT is not new. However, the use of 3D modeling for case-specific surgery planning is developing rapidly. There are many patients with posttraumatic

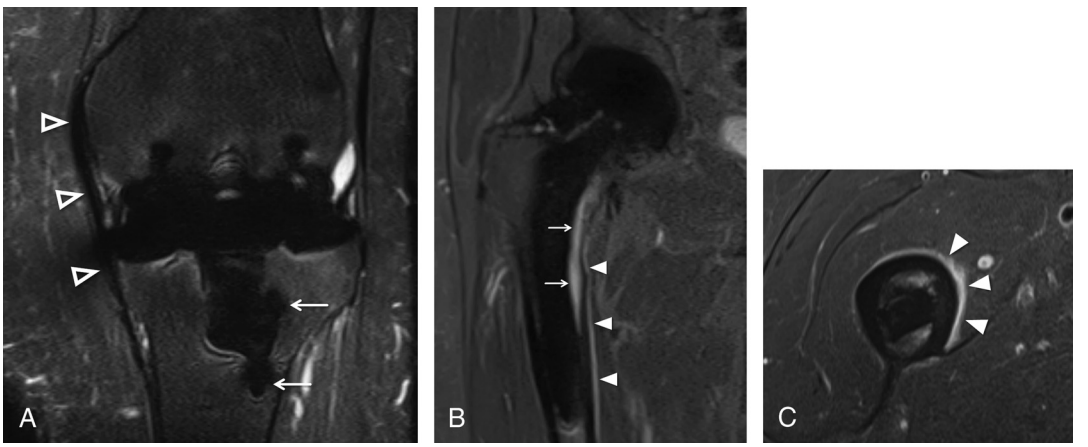

FIGURE 4. A, Coronal STIR SEMAC image in a patient with total arthroplasty of the left knee provides good image quality with homogeneous fat suppression even adjacent to the metal implants. The arthroplasty and the cortical screws (arrows) at the level of the proximal tibia are well delineated. The medial collateral ligament (outlined arrowheads) can be seen in its full length without being obscured by artifacts. B, Coronal STIR SEMAC image in a different patient with painful total arthroplasty of the right hip, with bone marrow edema (arrows) and periosteal edema (arrowheads) on the medial side of the femoral diaphysis. C, Axial STIR WARP image in the same patient as (B) at the tip of the prosthesis shaft also nicely shows the periosteal edema (arrowheads).

conditions that potentially could benefit from a patient-specific treatment planning, such as patients with malunion of wrist fractures.[130] Persistent osseous irregularities at the articular surfaces can lead to secondary OA and are a major predictor for a negative postoperative outcome. Thus, the preoperative detection and treatment of these irregularities is crucial.

Preoperative simulation of surgical procedures includes the following 3 major work steps (Fig. 5)[131] : First, a CT-based 3D reconstruction and segmentation of the affected bones is performed. If metal implants are to be used, they need to be segmented and a 3D model has to be generated for 3D surgery planning.

Second, decision making on the targeted bone shape is carried out. The intended postoperative bone shape heavily depends on preoperative conditions such as amount of bone loss, degree of malunion, and the specific anatomical circumstances such as vicinity to radial or ulnar vessels and nerves. Often, an anatomical reconstruction of the distal radius is impossible, and creative alternatives have to be considered. In many cases, a template generated from a mirrored 3D data set of the normal contralateral wrist is helpful. Superimposed 3D reconstructions of the abnormal wrist and the normal wrist often facilitate the understanding of posttraumatic deviations. Based on these 3D evaluations, the surgeons can find the optimal location and orientation of osteotomies and identify the translation needed between osseous chunks to restore a smooth distal radial joint surface.

As the final step, drilling and positioning guides are constructed to facilitate surgery and to assure optimal results. Therefore, the construction of patient-specific guides is a crucial step. The guides are generally printed on a 3D printer on site or delivered by a dedicated supplier of 3D printouts. On the contact surface with the distal radius, the drilling guide features the negative shape of the bone surface. This helps

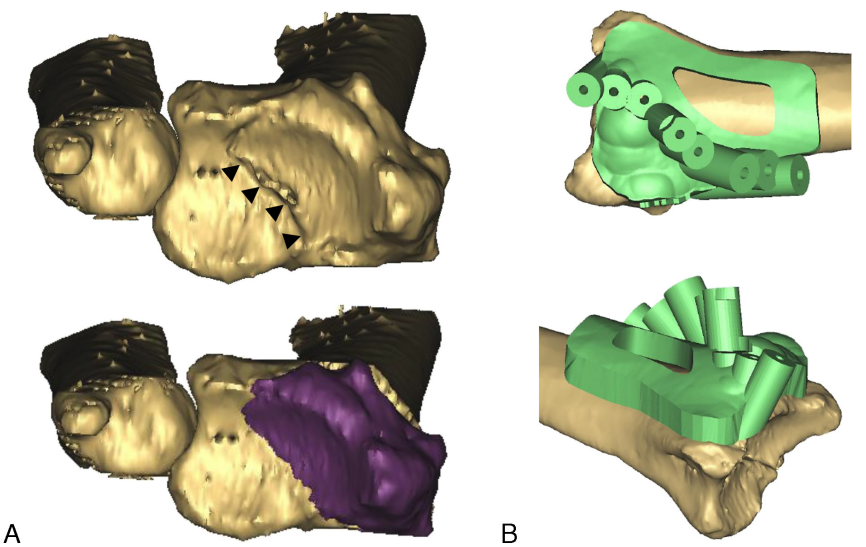

FIGURE 5. A, Three-dimensional reconstruction of the distal articular facet of the radius and malunion after fracture based on CT data. Upper part, There is marked osseous irregularity (arrowheads) along the prior fracture. Lower part, Targeted bone shape to restore a smooth joint surface. The purple bone chunk section has to be detached and reattached in a new position to close the gap and remove osseous irregularities. B, Patient-specific drilling block for obtaining the targeted bone shape in Figure 1A. The drilling holes serve to produce a predefined breaking line to detach the targeted bone chunk. Images courtesy of CARD Group Balgrist University Hospital. Figure 5 can be viewed online in color at www.investigativeradiology.com.

to correctly position the drilling block. The drilling holes in this block serve to produce a predefined breaking line. Once a bone chunk is detached during surgery, it is repositioned by the use of a positioning guide and attached in the new position by screws, plates, or other means of fixation.

Beyond correction of malunions of the distal radius, the technique previously described can also be used to understand more complex problems such as scaphoid fractures or posttraumatic restriction of pronation and supination caused by axis deviation.[132,133]

Automated Image Analysis in Radiographs of the Joints

In 1989, automated image analysis methods were presented for the first time for quantifying joint spaces in radiographs of the hand[134] and knee.[135] These initial methods required elaborate preprocessing steps, since a conversion from analog radiographs to a video signal and subsequent digitization was needed. The introduction of x-ray film scanners and later, fully digital x-ray systems, has made these automated image analyses much more applicable in practice. Although the literature on joint quantification based on MRI is more extensive owing to its high soft tissue contrast within the joints, radiographs still receive extensive interest from researchers today because of its practical availability, ease of use, and its high in-plane resolution, despite drawbacks of overprojection and lack of contrast between, for example, synovium and cartilage.

Most studies on joint quantification are focused on imaging biomarkers for rheumatoid arthritis (RA) and OA, measuring joint space narrowing as a surrogate marker of cartilage damage. Because of its size relative to image resolution and predominant occurrence of disease, the knee joint is the most frequently investigated by computerized analyses, followed by the joints in the hand and wrist, whereas the remaining joints are examined only rarely.

Based on automatically detected bone contours, different parameters can be deduced. By examining the distances between the proximal and distal bone contour of a joint, the mean or minimum joint space width (JSW) has been calculated, or a single between-contour distance at specific landmarks.[136] From the same contours, the joint space area can be computed by summing all contour distances,[137] and similarly, the area of osteophytes can be calculated semiautomatically.[138]For these measurements, image processing techniques have been used, initially based on simple edge detection algorithms and later, with the advent of more powerful computers, by more advanced techniques, like statistical shape models. Whereas JSW can in principle be measured in any joint, joint-specific features have also been defined, for example, the tibial eminence height.[138] Furthermore, disease-specific measurements have been developed, for example, JSW made independent of osteophyte growth in OA.[139] Finally, bony structures surrounding the joint have been assessed quantitatively by subchondral bone mineral densitometry, bone texture analysis, and measuring the subchondral cortical thickness, erosion size, and joint alignment.[140–143]

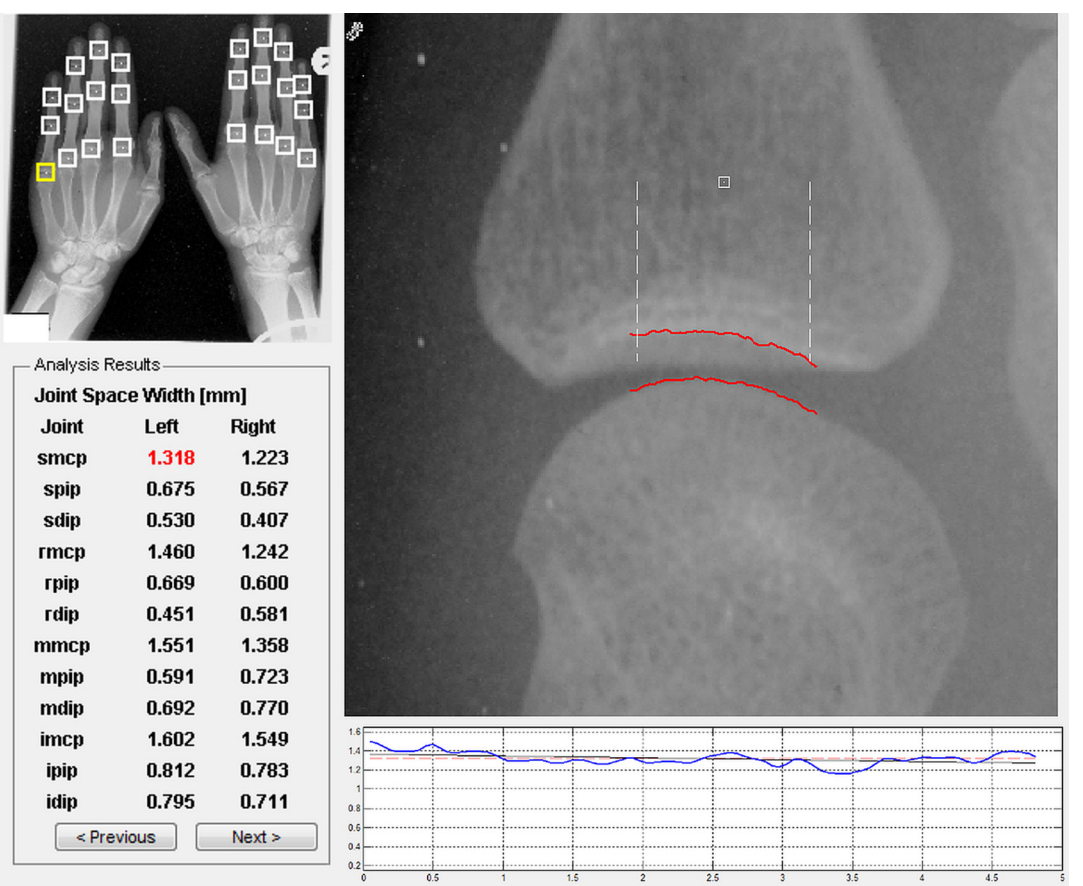

FIGURE 6. Automated image analysis of JSW of both hands on a screenshot of the user interface of the JAQ-program. In this step of the automated joint analysis, the user is able to adjust the detected contours by adding support points. The side panel shows the original hand radiograph, where the finger joint locations have been detected automatically. By selecting a joint in this image (small yellow rectangle), a close-up of the joint is presented in the main panel. The vertical dotted lines in the main panel indicate a standardized measurement area. After each optional adjustment, the calculated mean JSW is updated. The graph on the bottom shows the individual distances as a function of the horizontal position within the joint. Figure 6 can be viewed online in color at www.investigativeradiology.com.

In many of the aforementioned applications, image processing has helped automate these measurements, thereby improving objectivity and reproducibility. As a result, some clinical trials have been conducted for evaluation of drug efficacy, based on automated joint space measurements.[144] Different software packages have been developed, including AIDA / KIDA[138], KOACAD[145], CAJSA,[146] and JAQ[139], the latter of which can be downloaded for free for Matlab users (www.lkeb.nl/Software Downloads, Fig. 6). The validity of these automated quantification methods have been investigated in many studies on correlations with manual scoring of joint space narrowing, clinical outcome parameters, and biomarkers of disease activity. In addition, reproducibility has been evaluated through studies on interobserver/intraobserver variability[135] and interunit/intraunit variability.[147] In longitudinal studies, the sensitivity to change in the joint space has been validated, and for some measures, normal values have been established.[146]

As for any projection modality, patient positioning is a known source of error, as is radiographic magnification (especially in the knee, hip, and shoulder). Therefore, many researchers have studied the influence of patient positioning to produce an optimal imaging protocol for joint measurements. In a single-joint evaluation like the knee, positioning (flexion angle with respect to x-ray focus) has been optimized. With hand x-rays, however, it becomes impractical to do this for each joint separately. Adding 3D anatomical information in the automated joint assessment (ie, using 3D statistical shape models from CT)[148] may be useful in making the measurements less dependent on patient positioning. Better still, the recent development of clinical micro-CT might possibly give a more direct solution by providing high-resolution intrinsically of 3D data of the joints.[149,150]

Ultra Low-Dose Biplanar Radiographs

Orthopedic radiology is characterized by the need for increasingly precise imaging and measurement techniques to provide the referring surgeon with the necessary information for case-specific surgery and to track long-term posture changes in abnormalities such as degenerative spine disease and scoliosis. According to the "as low as reasonably achievable principle," a low radiation dose associated with the modality used is required, since the affected patients are often adolescents and children with the need for repetitive follow-up examinations.[151]

So-called biplanar x-ray scanners fulfill these requirements and are based on the concept of radiostereometric analysis, which is well known in the scientific literature since the 1990's: the position in space of an object is reconstructed from two 2D x-ray films.[152,153] The scientific setup used for those studies generally comprised either a single fluoroscopy device with images acquired at different angulations or 2 geometrically exactly aligned fluoroscopy devices for simultaneous acquisition of 2 projections.

The latter technique is used in a current all-in-one biplanar x-ray scanner (EOS) that allows acquiring low-dose biplanar x-rays (frontal and lateral views) in daily clinical work.[154] Imaging of the whole spine of a child in 2 planes (frontal and lateral views) using this technique leads to a radiation dose of approximately 358 μSv.[155] For comparison, the radiation dose of a whole spine examination in one plane using a conventional digital radiography system leads to a dose of approximately 1500 μSv.[155] Thanks to newly introduced hardware and software (the so-called MicroDose© technique), the radiation dose associated with a 2-plane spine scan in children can be even further reduced to approximately 58 μSv. This radiation is approximately equal to the radiation dose acquired while living on earth for one week (8 μSv per day).

Postprocessing of biplanar radiographs consists of assigning 3D coordinates to every point in the scanned volume. Three-dimensional models of the leg and spine can be generated by adjusting standardized 3D bone models to the osseous contours of a patient's frontal and lateral view radiographs. Based on these 3D models, complex 3D measurements become possible (Fig. 7). Length and angles can be measured in space or projected to a freely defined plane. However, it is important

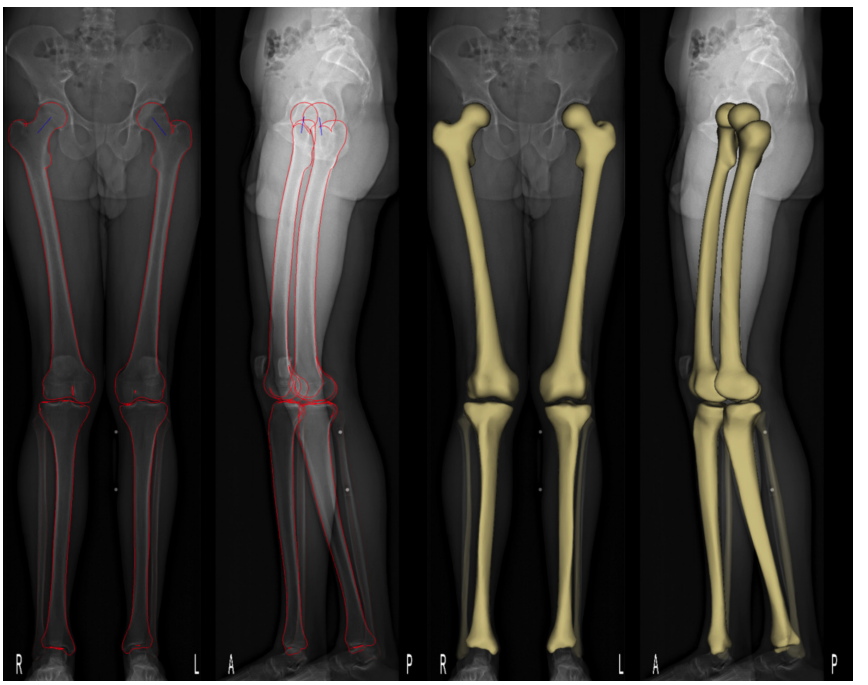

FIGURE 7. Three-dimensional reconstruction of the lower extremities based on ultra-low-dose biplanar radiographs. Bone models are manually adjusted to the osseous contours on the frontal and lateral radiograph (red lines on the left side of the figure). Upon identification of the osseous contour, the computer calculates a 3D model of the bones that is then superimposed on the original radiographs (right side of the figure). Additional measurement such as leg axis, leg length, and femoral and tibial torsion are generated automatically with this method. Figure 7 can be viewed online in color at www.investigativeradiology.com.

to keep in mind that such 3D models do not reflect 3D detailed anatomy. Therefore, fractures, tumors, and individual bone changes will not be visible when looking at the surface rendered 3D models of a patient.

Based on 3D models of the legs, there are several evaluations that can help the surgeon to monitor malposition over time or to prepare surgery. Limb length and axis can be measured in 3D with potential compensation for measurement errors on conventional 2D frontal radiographs owing to an extension deficit of the knee joint.[156–158] Following a simple step-by-step postprocessing procedure, it is also possible to measure femoral and tibial torsion in adults and children.[159–162]

Patients with scoliosis are generally examined periodically to monitor changes and to recognize the best time for corrective surgery. Additionally, postoperative follow-up examinations are often needed for long-term evaluation of treatment success.[163] Scoliosis parameters, such as Cobb angles and plumb line, can be measured on a single frontal view radiograph in a weight-bearing upright patient position. Alternatively, the sagittal balance of the spine, 3D scoliosis evaluation, and torsional changes of every single vertebral body can be evaluated based on a simultaneous acquisition of a frontal and lateral view radiograph.[157,164]

Currently, further applications for biplanar radiographs are being developed in various anatomical regions, such as the foot in patients with hindfoot malalignment, the hip in patients with FAI, or after total hip prosthesis implantation and patellofemoral maltracking disorders.

Magnetic Resonance Neurography

Over the past few years, a rapid evolution of MR neurography has been seen, with massively improved image quality and the possibility of detailed assessments of the plexuses, peripheral nerves, and their branches in the extremities (Fig. 8).[165]

Magnetic resonance neurography pulse sequences may be divided into nerve-nonselective, nerve-selective, and nerve-functional sequences. Nerve-nonselective sequences include standard 2D or isotropic 3D TSE sequences that provide standard T1 and T2 contrast weighting. The 2D sequences are usually acquired in a plane perpendicular to the long axis of the nerves, and their predominant value is in the detection of T2 signal abnormalities as well as in the evaluation of the fascicular structure of nerves.[166] Reconstruction of maximum intensity projection images from isotropic 3D sequences may be helpful for visualizing complex structures such as the brachial plexus (eg, thin slice maximum intensity projection images with a slice thickness of 2 cm).[167] Nerve-nonselective sequences are often combined with fat suppression, which can either be a spectral adiabatic inversion recovery, a STIR, or a Dixon-based technique. However, whatever technique is used, the uniformity of the fat suppression is of particular importance, since subtle T2 signal abnormalities might be the only sign of a peripheral neuropathy.[168] Nerve-selective sequences use diffusion weighting to suppress the background signal, that is, from vessels. An example for this type of sequences is the diffusion-based 3D reversed-FISP (DW-PSIF) sequence, which, unfortunately, has some limitations when large fields-of-view are needed, for example, in the plexuses.[169] For the latter, a recently developed method could be used as an alternative, the 3D (nerve-sheath signal increased with inked rest-tissue rapid acquisition with refocused echoes (RARE) imaging) technique, which combines a fat-suppression prepulse, improved motion-sensitized driven-equilibrium preparation to suppress the vessel signal, and 3D variable refocusing flip-angle RARE (rapid acquisition with refocused echoes) readout segments for contrast-efficient T2-weighted images.[170]

Nerve-functional imaging is based on diffusion-weighted imaging (DWI) and diffusion tensor imaging (DTI). Diffusion-weighted imaging and DTI both cross the border of morphological imaging as they provide functional information about peripheral nerves.[171–173] For both DWI and DTI, multiple numbers of excitation are often used to gain enough signal. Thus, current DWI and DTI applications come with long acquisition times, especially when larger fields-of-view are imaged. Soon, new accelerated techniques using SMS echo planar imaging with blipped CAIPIRINHA will be available. This development includes SMS imaging where multiple slices are excited concurrently with a multiband radiofrequency pulse, which translates into a substantial reduction in DWI and DTI imaging time.[174]

Interpretation of MR neurography images is considered to be complicated. However, considering some basic principles, many pitfalls can be avoided, and a reliable diagnosis can be made. First, the normal MR appearance of the nerve needs to be known. The proximal portions of a nerve are thicker than the distal portions. This means that any nerve thickening distally or any tortuous course of a nerve should raise one's attention with regard to possible neuropathy.[175] Second, normal nerves have a fascicular pattern that is best evaluated in T1- and T2-weighted images perpendicular to the long axis of a nerve. On high-resolution 3.0-T images, the fascicular pattern should always be visible, and in its absence, one should consider nerve pathology.[175–177] Third, peripheral nerves are typically surrounded by fat. Loss of this fat plane is a sign for pathology.[175] Fourth, some nerves show atypical courses such as penetration of muscles. These normal variants might be asymptomatic but can be a cause of entrapment syndromes. Fifth, the normal nerve signal is similar to the signal of adjacent skeletal muscles on T1- and T2-weighted pulse sequences with the exception of STIR and SPACE images, where the normal nerve signal is markedly higher than the surrounding tissue. Any increased signal intensity should raise the suspicion for neuropathy.[176] Sixth, artifacts from small metal implants such as clips at nearby veins may cause local field inhomogeneities resulting in focal absence of nerve signal. This is a typical pitfall for nerve discontinuity. Lastly, peripheral nerves are covered by the nerve-blood barrier, which means that normal peripheral nerves do not take up contrast agent. Therefore, any contrast enhancement is a clear sign of neuropathy and, for example, is frequently found in acute inflammation of plexuses.[165,175]

THE FUTURE OF MSK RADIOLOGY

In the final section of this article, we attempt to predict some of the developments that will shape MSK radiology in the next decades.

MRI Will Become Ultrafast

The acquisition time of MSK MRI examinations has been shortened considerably, since MRI was introduced in clinical routine imaging. This development will accelerate: MRI will become ultrafast, with, for example, comprehensive joint imaging being done within 3 minutes time. What are the technical innovations that will drive the acceleration of MRI? First, sparsity imaging/compressed sensing and techniques using a multiband radiofrequency pulse are expected to speed up acquisition times.[178] One field where this is already being implemented in MSK MRI is imaging of painful joint replacements.[127] To adequately suppress through-plane artifacts, very long acquisition times would be ideal for multispectral imaging. If such sequences can be acquired in a much shorter time, this will revolutionize MRI of metal implants. Second, MR fingerprinting and similar technologies will have a substantial impact on our specialty.[179,180] For example, a single multiparametric sequence is acquired and then used to calculate all standard weightings as well as T1 maps, T2 maps, DWI, etc. Similar to the current multidetector CT, the exact imaging planes will not need to be planned ahead, but rather, a 3D volume is acquired and then secondary multiplanar reconstructions are performed in any desired weighting. Furthermore, MRI with field strengths greater than 3 T will be routinely in use with dedicated MSK coils, providing a high SNR. Magnetic resonance imaging and CT arthrography will be replaced by high-resolution noncontrast imaging, with improved high-resolution 3D sequences for cartilage as well as the implementation of quantitative

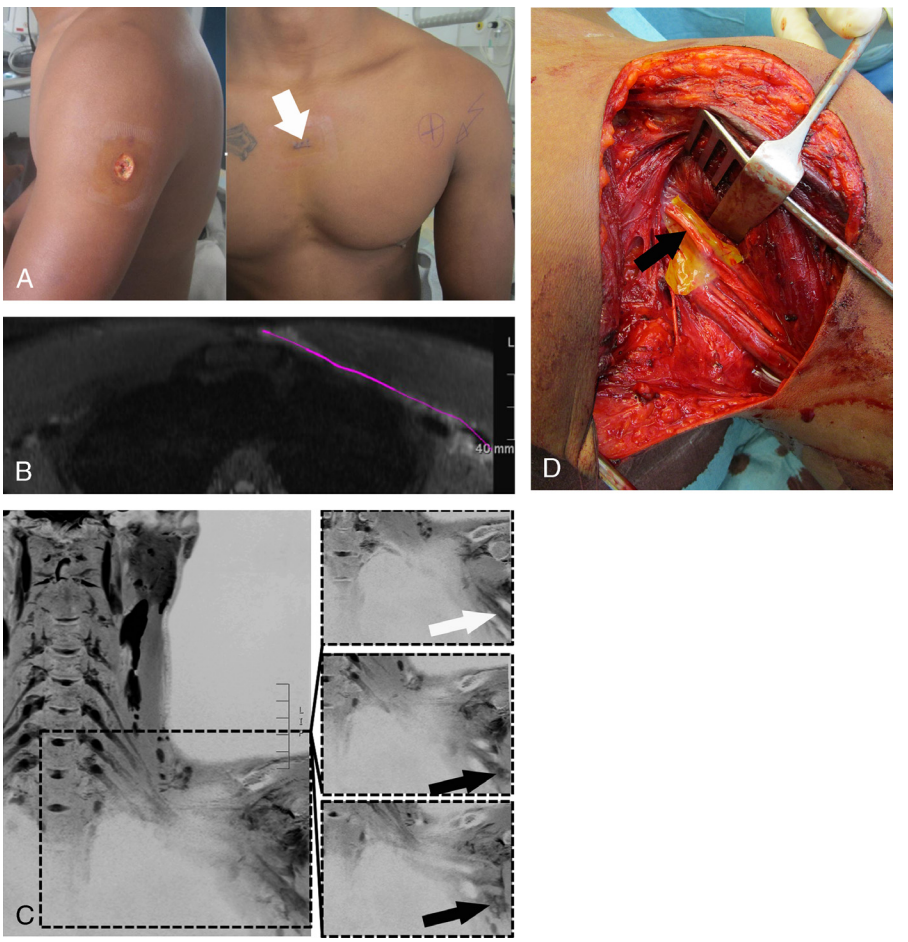

FIGURE 8. Twenty-four-year-old male patient with a gunshot wound. A, Photograph shows entry point of the bullet at the dorsal aspect of the left upper arm and the exit point at the sternum (arrow). Two days after the shooting, the patient developed loss of sensory and motor function in the median nerve region. Clinical and electrodiagnostic examination could not reveal nerve discontinuity, but owing to diffuse neuropathic pain, the patient was referred for MR neurography. B, Axial reconstruction from a 3D SPACE STIR sequence shows the course of the bullet through the upper thoracic region (purple line). No bleeding or lung injury was noted. C, Coronal reconstructions from a 3D SPACE STIR sequence shows the left brachial plexus (left overview image) with one normal (white arrow in enlarged display detail, right upper image) and 2 interrupted fascicles (black arrows in enlarged display details, right middle and lower image, respectively). D, Subsequent surgery confirmed the diagnosis, and sural nerve transplantation was performed with replacement of the 2 damaged fascicles (arrow). Figure 8 can be viewed online in color at www.investigativeradiology.com.

imaging biomarkers in clinical routine imaging. With ultrafast imaging, patient management will become the limiting factor for enhancing patient throughput. New ways of positioning patients in the scanner and coil management need to be developed.

MRI Will Become Semiautomated

Acquisition of MRI will be revolutionized. For a long time, the planning of MRI sequences has been tedious and sometimes complicated. With advanced technology, it will be possible to position the patient on the examination table, select a specific MRI program, and press the start button. It will be possible to modify specific examination parameters manually, but the scanner evaluates patient habitus and artifact profile and correctly chooses the right examination parameters for standard MSK examinations. The evaluation of the MRI examination will still need human attention and focus, but some aspects of assessing the MR images will become semiautomated, such as orthopedic standard measurements or tumor follow-up measurements.[181]

Mega-Trends in MSK Research

What are the developments in research? Personalized medicine will transform our health system within the next 50 years, and this will also affect radiology. Biobanks with many layers of patient-based imaging data will be implemented and cross-linked to clinical and genetic data.[182] Individual imaging data will be matched to standardized data from healthy and diseased individuals to allow automated quantitative assessment of tissues. Data mining will allow investigating the effectiveness of MSK radiology and the impact that imaging is having on patient outcome.

CONCLUSION

In this article, we assessed the patterns of innovation that were essential for the transformation of MSK imaging since 50 years ago, when *Investigative Radiology* was established as a journal. The state-of-the-art joint imaging of 2015 has been exemplified through 9 key concepts, including cutting-edge clinical applications and topics at the forefront of MSK research. Lastly, we attempted to predict some of the developments that will shape MSK radiology in the future.

ACKNOWLEDGMENTS

The authors thank Michael Recht, MD (NYU Langone Medical Center, New York, NY), Mini Pathria, MD (University of California-San Diego, San Diego, CA), Thomas Böni, MD (Balgrist University

Hospital, Zurich, Switzerland), and Siegfried Trattnig, MD (Medical University of Vienna, Vienna, Austria), for their input regarding the history and future of MSK imaging. Furthermore, the authors thank the Computer Assisted Research & Development (CARD) Group of Balgrist University Hospital, Zurich, Switzerland, for counseling and supply of Figure 5.

REFERENCES

1. Genant HK, Doi K, Mall JC. Comparison of non-screen techniques (medical vs. industrial film) for fine-detail skeletal radiography. *Invest Radiol*. 1976;11: 486–500.
2. Engelstad BL, Friedman EM, Murphy WA. Diagnosis of joint effusion on lateral and axial projections of the knee. *Invest Radiol*. 1981;16:188–192.
3. Spataro RF, Katzberg RW, Burgener FA, et al. Epinephrine enhanced knee arthrography. *Invest Radiol*. 1978;13:286–290.
4. Resnick D, Kerr R, Andre M, et al. Digital arthrography in the evaluation of painful joint prostheses. *Invest Radiol*. 1984;19:432–437.
5. Grechenig W, Peicha G, Fellinger M, et al. Wrist arthrography after acute trauma to the distal radius: diagnostic accuracy, technique, and sources of diagnostic errors. *Invest Radiol*. 1998;33:273–278.
6. Resnick D, Sartoris DJ. The status of osteoradiology fellowship training in the United States. *AJR Am J Roentgenol*. 1987;149:973–974.
7. Langen HJ, Klein HM, Wein B, et al. Comparative evaluation of digital radiography versus conventional radiography of fractured skulls. *Invest Radiol*. 1993; 28:686–689.
8. Andresen R, Radmer S, Sparmann M, et al. Imaging of hamate bone fractures in conventional X-rays and high-resolution computed tomography. An in vitro study. *Invest Radiol*. 1999;34:46–50.
9. Martinez S, Korobkin M, Fondren FB, et al. Computed tomography of the normal patellofemoral joint. *Invest Radiol*. 1983;18:249–253.
10. Cone RO, Szabo R, Resnick D, et al. Computed tomography of the normal radioulnar joints. *Invest Radiol*. 1983;18:541–545.
11. Pavlov H, Freiberger RH, Deck MF, et al. Computer-assisted tomography of the knee. *Invest Radiol*. 1978;13:57–62.
12. Fishman EK, Ney DR, Kawashima A, et al. Effect of image display on the quality of multiplanar reconstruction of computed tomography data. *Invest Radiol*. 1993;28:146–149.
13. Levy RA, Kellman RM, Rosenbaum AE. The effect of computed tomographic scan orientation on information loss in the three-dimensional reconstruction of tripod zygomatic fractures. *Invest Radiol*. 1991;26:427–431.
14. McEnery KW, Wilson AJ, Murphy WA Jr. Comparison of spiral computed tomography versus conventional computed tomography multiplanar reconstructions of a fracture displacement phantom. *Invest Radiol*. 1994;29:665–670.
15. Farin PU, Kaukanen E, Jaroma H, et al. Site and size of rotator-cuff tear. Findings at ultrasound, double-contrast arthrography, and computed tomography arthrography with surgical correlation. *Invest Radiol*. 1996;31:387–394.
16. Blum AG, Simon JM, Cotten A, et al. Comparison of double-contrast CT arthrography image quality with nonionic contrast agents: isotonic dimeric iodixanol 270 mg I/mL and monomeric iohexol 300 mg I/mL. *Invest Radiol*. 2000;35:304–310.
17. Mansfield P, Maudsley AA. Medical imaging by NMR. *Br J Radiol*. 1977;50: 188–194.
18. Crooks LE, Grover TP, Kaufman L, et al. Tomographic imaging with nuclear magnetic resonance. *Invest Radiol*. 1978;13:63–66.
19. Polak JF, Jolesz FA, Adams DF. Magnetic resonance imaging of skeletal muscle. Prolongation of T1 and T2 subsequent to denervation. *Invest Radiol*. 1988;23: 365–369.
20. Fisher MJ, Meyer RA, Adams GR, et al. Direct relationship between proton T2 and exercise intensity in skeletal muscle MR images. *Invest Radiol*. 1990;25: 480–485.
21. Ho C, Cervilla V, Kjellin I, et al. Magnetic resonance imaging in assessing cartilage changes in experimental osteoarthrosis of the knee. *Invest Radiol*. 1992;27: 84–90.
22. Hodgson RJ, Barry MA, Carpenter TA, et al. Magnetic resonance imaging protocol optimization for evaluation of hyaline cartilage in the distal interphalangeal joint of fingers. *Invest Radiol*. 1995;30:522–531.
23. Trattnig S, Mlynarik V, Huber M, et al. Magnetic resonance imaging of articular cartilage and evaluation of cartilage disease. *Invest Radiol*. 2000;35:595–601.
24. Welsch GH, Zak L, Mamisch TC, et al. Three-dimensional magnetic resonance observation of cartilage repair tissue (MOCART) score assessed with an isotropic three-dimensional true fast imaging with steady-state precession sequence at 3.0 Tesla. *Invest Radiol*. 2009;44:603–612.
25. Allmann KH, Walter O, Laubenberger J, et al. Magnetic resonance diagnosis of the anterior labrum and capsule. Effect of field strength on efficacy. *Invest Radiol*. 1998;33:415–420.
26. Allmann KH, Schafer O, Hauer M, et al. Indirect MR arthrography of the unexercised glenohumeral joint in patients with rotator cuff tears. *Invest Radiol*. 1999; 34:435–440.
27. Weishaupt D, Zanetti M, Tanner A, et al. Lesions of the reflection pulley of the long biceps tendon. MR arthrographic findings. *Invest Radiol*. 1999;34: 463–469.
28. Zanetti M, Gerber C, Hodler J. Quantitative assessment of the muscles of the rotator cuff with magnetic resonance imaging. *Invest Radiol*. 1998;33:163–170.
29. van de Sande MA, Stoel BC, Obermann WR, et al. Quantitative assessment of fatty degeneration in rotator cuff muscles determined with computed tomography. *Invest Radiol*. 2005;40:313–319.
30. Boxheimer L, Lutz AM, Treiber K, et al. MR imaging of the knee: position related changes of the menisci in asymptomatic volunteers. *Invest Radiol*. 2004; 39:254–263.
31. Hajek PC, Gylys-Morin VM, Baker LL, et al. The high signal intensity meniscus of the knee. Magnetic resonance evaluation and in vivo correlation. *Invest Radiol*. 1987;22:883–890.
32. Englund M, Guermazi A, Gale D, et al. Incidental meniscal findings on knee MRI in middle-aged and elderly persons. *N Engl J Med*. 2008;359:1108–1115.
33. Zanetti M, Pfirrmann CW, Schmid MR, et al. Patients with suspected meniscal tears: prevalence of abnormalities seen on MRI of 100 symptomatic and 100 contralatera
l asymptomatic knees. *AJR Am J Roentgenol*. 2003;181:635–641.
34. Boks SS, Vroegindeweij D, Koes BW, et al. Magnetic resonance imaging abnormalities in symptomatic and contralateral knees: prevalence and associations with traumatic history in general practice. *Am J Sports Med*. 2006;34: 1984–1991.
35. Ganz R, Parvizi J, Beck M, et al. Femoroacetabular impingement: a cause for osteoarthritis of the hip. *Clin Orthop Relat Res*. 2003;417:112–120.
36. Sutter R, Dietrich TJ, Zingg PO, et al. How useful is the alpha angle for discriminating between symptomatic patients with cam-type femoroacetabular impingement and asymptomatic volunteers? *Radiology*. 2012;264:514–521.
37. Hartzman S, Gold RH, Bassett LW. 1.5-T surface-coil MRI of the knee. *Invest Radiol*. 1987;22:847–848.
38. Scheidler J, Heuck AF, Bruening R, et al. Magnetic resonance imaging of the female pelvis. New circularly polarized body array coil versus standard body coil. *Invest Radiol*. 1997;32:1–6.
39. Ai T, Morelli JN, Hu X, et al. A historical overview of magnetic resonance imaging, focusing on technological innovations. *Invest Radiol*. 2012;47:725–741.
40. Jaramillo D, Laor T, Mulkern RV. Comparison between fast spin-echo and conventional spin-echo imaging of normal and abnormal musculoskeletal structures in children and young adults. *Invest Radiol*. 1994;29:803–811.
41. Hilfiker P, Zanetti M, Debatin JF, et al. Fast spin-echo inversion-recovery imaging versus fast T2-weighted spin-echo imaging in bone marrow abnormalities. *Invest Radiol*. 1995;30:110–114.
42. Lenkinski RE, Listerud J, Shinkwin MA, et al. Magnetic resonance imaging and magnetic resonance spectroscopy of bone tumors and bone marrow disease. *Invest Radiol*. 1989;24:1006–1010.
43. Koblik PD, Freeman DM. Short echo time magnetic resonance imaging of tendon. *Invest Radiol*. 1993;28:1095–1100.
44. Ai T, Padua A, Goerner F, et al. SEMAC-VAT and MSVAT-SPACE sequence strategies for metal artifact reduction in 1.5 T magnetic resonance imaging. *Invest Radiol*. 2012;47:267–276.
45. Notohamiprodjo M, Horng A, Pietschmann MF, et al. MRI of the knee at 3 T: first clinical results with an isotropic PDfs-weighted 3D-TSE-sequence. *Invest Radiol*. 2009;44:585–597.
46. Mlynarik V, Trattnig S. Physicochemical properties of normal articular cartilage and its MR appearance. *Invest Radiol*. 2000;35:589–594.
47. Kimelman T, Vu A, Storey P, et al. Three-dimensional T1 mapping for dGEMRIC at 3.0 T using the Look Locker method. *Invest Radiol*. 2006;41: 198–203.
48. Bolbos RI, Ma CB, Link TM, et al. In vivo T1rho quantitative assessment of knee cartilage after anterior cruciate ligament injury using 3 Tesla magnetic resonance imaging. *Invest Radiol*. 2008;43:782–788.
49. Bittersohl B, Hosalkar HS, Werlen S, et al. Intravenous versus intra-articular delayed gadolinium-enhanced magnetic resonance imaging in the hip joint: a comparative analysis. *Invest Radiol*. 2010;45:538–542.
50. Welsch GH, Mamisch TC, Hughes T, et al. In vivo biochemical 7.0 Tesla magnetic resonance: preliminary results of dGEMRIC, zonal T2, and T2* mapping of articular cartilage. *Invest Radiol*. 2008;43:619–626.

51. Krug R, Stehling C, Kelley DA, et al. Imaging of the musculoskeletal system in vivo using ultra-high field magnetic resonance at 7 T. *Invest Radiol*. 2009;44: 613–618.
52. Zbyn S, Brix MO, Juras V, et al. Sodium magnetic resonance imaging of ankle joint in cadaver specimens, volunteers, and patients after different cartilage repair techniques at 7 T: initial results. *Invest Radiol*. 2015;50:246–254.
53. Wang Y. Description of parallel imaging in MRI using multiple coils. *Magn Reson Med*. 2000;44:495–499.
54. Breuer FA, Kellman P, Griswold MA, et al. Dynamic autocalibrated parallel imaging using temporal GRAPPA (TGRAPPA). *Magn Reson Med*. 2005;53: 981–985.
55. Ryan M, Cunningham P, Cantwell C, et al. A comparison of fast MRI of hips with and without parallel imaging using SENSE. *Br J Radiol*. 2005;78:299–302.
56. Kato Y, Higano S, Tamura H, et al. Usefulness of contrast-enhanced T1-weighted sampling perfection with application-optimized contrasts by using different flip angle evolutions in detection of small brain metastasis at 3 T MR imaging: comparison with magnetization-prepared rapid acquisition of gradient echo imaging. *AJNR Am J Neuroradiol*. 2009;30:923–929.
57. Milewski MD, Smitaman E, Moukaddam H, et al. Comparison of 3D vs. 2D fast spin echo imaging for evaluation of articular cartilage in the knee on a 3-T system scientific research. *Eur J Radiol*. 2012;81:1637–1643.
58. Jung JY, Jee WH, Park MY, et al. Meniscal tear configurations: categorization with 3D isotropic turbo spin-echo MRI compared with conventional MRI at 3 T. *AJR Am J Roentgenol*. 2012;198:W173–W180.
59. Kloth JK, Winterstein M, Akbar M, et al. Comparison of 3D turbo spin-echo SPACE sequences with conventional 2D MRI sequences to assess the shoulder joint. *Eur J Radiol*. 2014;83:1843–1849.
60. Tian CY, Shang Y, Zheng ZZ. Glenoid bone lesions: comparison between 3D VIBE images in MR arthrography and nonarthrographic MSCT. *J Magn Reson Imaging*. 2012;36:231–236.
61. Michaely HJ, Morelli JN, Budjan J, et al. CAIPIRINHA-Dixon-TWIST (CDT)-volume-interpolated breath-hold examination (VIBE): a new technique for fast time-resolved dynamic 3-dimensional imaging of the abdomen with high spatial resolution. *Invest Radiol*. 2013;48:590–597.
62. Breuer FA, Blaimer M, Heidemann RM, et al. Controlled aliasing in parallel imaging results in higher acceleration (CAIPIRINHA) for multi-slice imaging. *Magn Reson Med*. 2005;53:684–691.
63. Blaimer M, Choli M, Jakob PM, et al. Multiband phase-constrained parallel MRI. *Magn Reson Med*. 2013;69:974–980.
64. Larkman DJ, Hajnal JV, Herlihy AH, et al. Use of multicoil arrays for separation of signal from multiple slices simultaneously excited. *J Magn Reson Imaging*. 2001;13:313–317.
65. Feinberg DA, Setsompop K. Ultra-fast MRI of the human brain with simultaneous multi-slice imaging. *J Magn Reson*. 2013;229:90–100.
66. Vasanawala S, Murphy M, Alley M, et al. Practical parallel imaging compressed sensing MRI: summary of two years of experience in accelerating body MRI of pediatric patients. *Proc IEEE Int Symp Biomed Imaging*. 2011;2011:1039–1043.
67. Sutter R, Zanetti M, Pfirrmann CW. New developments in hip imaging. *Radiology*. 2012;264:651–667.
68. Beck M, Kalhor M, Leunig M, et al. Hip morphology influences the pattern of damage to the acetabular cartilage: femoroacetabular impingement as a cause of early osteoarthritis of the hip. *J Bone Joint Surg Br*. 2005;87:1012–1018.
69. Pfirrmann CW, Mengiardi B, Dora C, et al. Cam and pincer femoroacetabular impingement: characteristic MR arthrographic findings in 50 patients. *Radiology*. 2006;240:778–785.
70. Werner CM, Copeland CE, Stromberg J, et al. Correlation of the cross-over ratio of the cross-over sign on conventional pelvic radiographs with computed tomography retroversion measurements. *Skeletal Radiol*. 2010;39:655–660.
71. Notzli HP, Wyss TF, Stoecklin CH, et al. The contour of the femoral head-neck junction as a predictor for the risk of anterior impingement. *J Bone Joint Surg Br*. 2002;84:556–560.
72. Agricola R, Waarsing JH, Thomas GE, et al. Cam impingement: defining the presence of a cam deformity by the alpha angle: data from the CHECK cohort and Chingford cohort. *Osteoarthritis Cartilage*. 2014;22:218–225.
73. Ehrmann C, Rosskopf AB, Pfirrmann CW, et al. Beyond the alpha angle: alternative measurements for quantifying cam-type deformities in femoroacetabular impingement. *J Magn Reson Imaging*. 2015. [Epub ahead of print].
74. Kolo FC, Charbonnier C, Pfirrmann CW, et al. Extreme hip motion in professional ballet dancers: dynamic and morphological evaluation based on magnetic resonance imaging. *Skeletal Radiol*. 2013;42:689–698.
75. Sutter R, Dietrich TJ, Zingg PO, et al. Femoral antetorsion: comparing asymptomatic volunteers and patients with femoroacetabular impingement. *Radiology*. 2012;263:475–483.
76. Tibor LM, Liebert G, Sutter R, et al. Two or more impingement and/or instability deformities are often present in patients with hip pain. *Clin Orthop Relat Res*. 2013;471:3762–3773.
77. Yamamoto Y, Tonotsuka H, Ueda T, et al. Usefulness of radial contrast-enhanced computed tomography for the diagnosis of acetabular labrum injury. *Arthroscopy*. 2007;23:1290–1294.
78. Smith TO, Hilton G, Toms AP, et al. The diagnostic accuracy of acetabular labral tears using magnetic resonance imaging and magnetic resonance arthrography: a meta-analysis. *Eur Radiol*. 2011;21:863–874.
79. Sutter R, Zubler V, Hoffmann A, et al. Hip MRI: how useful is intraarticular contrast material for evaluating surgically proven lesions of the labrum and articular cartilage? *AJR Am J Roentgenol*. 2014;202:160–169.
80. Kijowski R. Clinical cartilage imaging of the knee and hip joints. *AJR Am J Roentgenol*. 2010;195:618–628.
81. Mintz DN, Hooper T, Connell D, et al. Magnetic resonance imaging of the hip: detection of labral and chondral abnormalities using noncontrast imaging. *Arthroscopy*. 2005;21:385–393.
82. Siversson C, Akhondi-Asl A, Bixby S, et al. Three-dimensional hip cartilage quality assessment of morphology and dGEMRIC by planar maps and automated segmentation. *Osteoarthritis Cartilage*. 2014;22:1511–1515.
83. Akella SV, Regatte RR, Gougoutas AJ, et al. Proteoglycan-induced changes in T1rho-relaxation of articular cartilage at 4 T. *Magn Reson Med*. 2001;46: 419–423.
84. Klocke NF, Amendola A, Thedens DR, et al. Comparison of T1rho, dGEMRIC, and quantitative T2 MRI in preoperative ACL rupture patients. *Acad Radiol*. 2013;20:99–107.
85. Pan J, Pialat JB, Joseph T, et al. Knee cartilage T2 characteristics and evolution in relation to morphologic abnormalities detected at 3-T MR imaging: a longitudinal study of the normal control cohort from the Osteoarthritis Initiative. *Radiology*. 2011;261:507–515.
86. Wang L, Regatte RR. Quantitative mapping of human cartilage at 3.0 T: parallel changes in T(2), T(1)rho, and dGEMRIC. *Acad Radiol*. 2014;21:463–471.
87. Maier CF, Tan SG, Hariharan H, et al. T2 quantitation of articular cartilage at 1.5 T. *J Magn Reson Imaging*. 2003;17:358–364.
88. Apprich S, Welsch GH, Mamisch TC, et al. Detection of degenerative cartilage disease: comparison of high-resolution morphological MR and quantitative T2 mapping at 3.0 Tesla. *Osteoarthritis Cartilage*. 2010;18:1211–1217.
89. Mosher TJ, Liu Y, Torok CM. Functional cartilage MRI T2 mapping: evaluating the effect of age and training on knee cartilage response to running. *Osteoarthritis Cartilage*. 2010;18:358–364.
90. Bittersohl B, Hosalkar HS, Hughes T, et al. Feasibility of T2* mapping for the evaluation of hip joint cartilage at 1.5 T using a three-dimensional (3D), gradient-echo (GRE) sequence: a prospective study. *Magn Reson Med*. 2009; 62:896–901.
91. Johannessen W, Auerbach JD, Wheaton AJ, et al. Assessment of human disc degeneration and proteoglycan content using T1rho-weighted magnetic resonance imaging. *Spine (Phila Pa 1976)*. 2006;31:1253–1257.
92. Pakin SK, Xu J, Schweitzer ME, et al. Rapid 3D-T1rho mapping of the knee joint at 3.0 T with parallel imaging. *Magn Reson Med*. 2006;56:563–571.
93. Wang L, Chang G, Xu J, et al. T1rho MRI of menisci and cartilage in patients with osteoarthritis at 3 T. *Eur J Radiol*. 2012;81:2329–2336.
94. Buck FM, Bae WC, Diaz E, et al. Comparison of T1rho measurements in agarose phantoms and human patellar cartilage using 2D multislice spiral and 3D magnetization prepared partitioned k-space spoiled gradient-echo snapshot techniques at 3 T. *AJR Am J Roentgenol*. 2011;196:W174–W179.
95. Gold GE, Chen CA, Koo S, et al. Recent advances in MRI of articular cartilage. *AJR Am J Roentgenol*. 2009;193:628–638.
96. Bashir A, Gray ML, Boutin RD, et al. Glycosaminoglycan in articular cartilage: in vivo assessment with delayed Gd(DTPA)(2-)-enhanced MR imaging. *Radiology*. 1997;205:551–558.
97. Endo J, Watanabe A, Sasho T, et al. Utility of T2 mapping and dGEMRIC for evaluation of cartilage repair after allograft chondrocyte implantation in a rabbit model. *Osteoarthritis Cartilage*. 2015;23:280–288.
98. Lesperance LM, Gray ML, Burstein D. Determination of fixed charge density in cartilage using nuclear magnetic resonance. *J Orthop Res*. 1992;10:1–13.
99. Lard LR, Visser H, Speyer I, et al. Early versus delayed treatment in patients with recent-onset rheumatoid arthritis: comparison of two cohorts who received different treatment strategies. *Am J Med*. 2001;111:446–451.
100. Ejbjerg B, McQueen F, Lassere M, et al. The EULAR-OMERACT rheumatoid arthritis MRI reference image atlas: the wrist joint. *Ann Rheum Dis*. 2005;64 (suppl 1):i23–i47.
101. Conaghan P, Bird P, Ejbjerg B, et al. The EULAR-OMERACT rheumatoid arthritis MRI reference image atlas: the metacarpophalangeal joints. *Ann Rheum Dis*. 2005;64(suppl 1):i11–i21.

102. Hetland ML, Ejbjerg B, Horslev-Petersen K, et al. MRI bone oedema is the strongest predictor of subsequent radiographic progression in early rheumatoid arthritis. Results from a 2-year randomised controlled trial (CIMESTRA). *Ann Rheum Dis*. 2009;68:384–390.
103. Peterfy CG, Countryman P, Gabriele A, et al. Magnetic resonance imaging in rheumatoid arthritis clinical trials: emerging patterns based on recent experience. *J Rheumatol*. 2011;38:2023–2030.
104. Duer-Jensen A, Horslev-Petersen K, Hetland ML, et al. Bone edema on magnetic resonance imaging is an independent predictor of rheumatoid arthritis development in patients with early undifferentiated arthritis. *Arthritis Rheum*. 2011;63: 2192–2202.
105. Olech E, Crues JV 3rd, Yocum DE, et al. Bone marrow edema is the most specific finding for rheumatoid arthritis (RA) on noncontrast magnetic resonance imaging of the hands and wrists: a comparison of patients with RA and healthy controls. *J Rheumatol*. 2010;37:265–274.
106. Ostergaard M, Edmonds J, McQueen F, et al. An introduction to the EULAR-OMERACT rheumatoid arthritis MRI reference image atlas. *Ann Rheum Dis*. 2005;64(Suppl 1):i3–i7.
107. Dohn UM, Ejbjerg BJ, Hasselquist M, et al. Detection of bone erosions in rheumatoid arthritis wrist joints with magnetic resonance imaging, computed tomography and radiography. *Arthritis Res Ther*. 2008;10:R25.
108. Kosta PE, Voulgari PV, Zikou AK, et al. The usefulness of magnetic resonance imaging of the hand and wrist in very early rheumatoid arthritis. *Arthritis Res Ther*. 2011;13:R84.
109. Cimmino MA, Innocenti S, Livrone F, et al. Dynamic gadolinium-enhanced magnetic resonance imaging of the wrist in patients with rheumatoid arthritis can discriminate active from inactive disease. *Arthritis Rheum*. 2003;48: 1207–1213.
110. Borrero CG, Mountz JM, Mountz JD. Emerging MRI methods in rheumatoid arthritis. *Nat Rev Rheumatol*. 2011;7:85–95.
111. Eshed I, Feist E, Althoff CE, et al. Tenosynovitis of the flexor tendons of the hand detected by MRI: an early indicator of rheumatoid arthritis. *Rheumatology (Oxford)*. 2009;48:887–891.
112. Schoellnast H, Deutschmann HA, Hermann J, et al. Psoriatic arthritis and rheumatoid arthritis: findings in contrast-enhanced MRI. *AJR Am J Roentgenol*. 2006;187:351–357.
113. Schwenzer NF, Kotter I, Henes JC, et al. The role of dynamic contrast-enhanced MRI in the differential diagnosis of psoriatic and rheumatoid arthritis. *AJR Am J Roentgenol*. 2010;194:715–720.
114. Boyesen P, McQueen FM, Gandjbakhch F, et al. The OMERACT Psoriatic Arthritis Magnetic Resonance Imaging Score (PsAMRIS) is reliable and sensitive to change: results from an OMERACT workshop. *J Rheumatol*. 2011;38: 2034–2038.
115. Hofmann S, Seitlinger G, Djahani O, et al. The painful knee after TKA: a diagnostic algorithm for failure analysis. *Knee Surg Sports Traumatol Arthrosc*. 2011;19:1442–1452.
116. Grubl A, Marker M, Brodner W, et al. Long-term follow-up of metal-on-metal total hip replacement. *J Orthop Res*. 2007;25:841–848.
117. Campbell P, Ebramzadeh E, Nelson S, et al. Histological features of pseudotumor-like tissues from metal-on-metal hips. *Clin Orthop Relat Res*. 2010;468:2321–2327.
118. Anderson H, Toms AP, Cahir JG, et al. Grading the severity of soft tissue changes associated with metal-on-metal hip replacements: reliability of an MR grading system. *Skeletal Radiol*. 2011;40:303–307.
119. Miller TT. Imaging of joint replacements. *Semin Musculoskelet Radiol*. 2015;19:1–2.
120. Pfirrmann CW, Notzli HP, Dora C, et al. Abductor tendons and muscles assessed at MR imaging after total hip arthroplasty in asymptomatic and symptomatic patients. *Radiology*. 2005;235:969–976.
121. Agten CA, Del Grande F, Fucentese SF, et al. Unicompartmental knee arthroplasty MRI: impact of slice-encoding for metal artefact correction MRI on image quality, findings and therapy decision. *Eur Radiol*. 2015. [Epub ahead of print].
122. Hargreaves BA, Worters PW, Pauly KB, et al. Metal-induced artifacts in MRI. *AJR Am J Roentgenol*. 2011;197:547–555.
123. Ulbrich EJ, Sutter R, Aguiar RF, et al. STIR sequence with increased receiver bandwidth of the inversion pulse for reduction of metallic artifacts. *AJR Am J Roentgenol*. 2012;199:W735–W742.
124. Koch KM, Lorbiecki JE, Hinks RS, et al. A multispectral three-dimensional acquisition technique for imaging near metal implants. *Magn Reson Med*. 2009;61: 381–390.
125. Sutter R, Ulbrich EJ, Jellus V, et al. Reduction of metal artifacts in patients with total hip arthroplasty with slice-encoding metal artifact correction and view-angle tilting MR imaging. *Radiology*. 2012;265:204–214.
126. Sutter R, Hodek R, Fucentese SF, et al. Total knee arthroplasty MRI featuring slice-encoding for metal artifact correction: reduction of artifacts for STIR and proton density-weighted sequences. *AJR Am J Roentgenol*. 2013;201: 1315–1324.
127. Nittka M, Otazo R, Rybak LD, et al. Highly accelerated SEMAC metal implant imaging using joint compressed sensing and parallel imaging. In: International Society for Magnetic Resonance in Medicine, 21st Annual Meeting and Exhibition, Salt Lake City, UT. 2013:2558.
128. Bachschmidt TJ, Sutter R, Jakob PM, et al. Knee implant imaging at 3 Tesla using high-bandwidth radiofrequency pulses. *J Magn Reson Imaging*. 2014. [Epub ahead of print].
129. Gutierrez LB, Do BH, Gold GE, et al. MR imaging near metallic implants using MAVRIC SL: initial clinical experience at 3 T. *Acad Radiol*. 2015;22:370–379.
130. Schweizer A, Furnstahl P, Nagy L. Three-dimensional correction of distal radius intra-articular malunions using patient-specific drill guides. *J Hand Surg Am*. 2013;38:2339–2347.
131. Furnstahl P, Schweizer A, Graf M, et al. Surgical treatment of long-bone deformities: 3D preoperative planning and patient-specific instrumentation. In: Zhen G, Li S, eds. *Lecture Notes in Computational Vision and Biomechanics. Computational Radiology for Orthopedic Interventions*. Springer, in press.
132. Schweizer A, Furnstahl P, Nagy L. Three-dimensional computed tomographic analysis of 11 scaphoid waist nonunions. *J Hand Surg Am*. 2012;37:1151–1158.
133. Furnstahl P, Schweizer A, Nagy L, et al. A morphological approach to the simulation of forearm motion. *Conf Proc IEEE Eng Med Biol Soc*. 2009:7168–7171.
134. Allander E, Forsgren PO, Pettersson H, et al. Computerized assessment of radiological changes of the hand in rheumatic diseases. *Scand J Rheumatol*. 1989;18: 291–296.
135. Dacre JE, Huskisson EC. The automatic assessment of knee radiographs in osteoarthritis using digital image analysis. *Br J Rheumatol*. 1989;28:506–510.
136. Hellio Le Graverand MP, Mazzuca S, Duryea J, et al. Radiographic-based grading methods and radiographic measurement of joint space width in osteoarthritis. *Radiol Clin North Am*. 2009;47:567–579.
137. Gordon CL, Wu C, Peterfy CG, et al. Automated measurement of radiographic hip joint-space width. *Med Phys*. 2001;28:267–277.
138. Marijnissen AC, Vincken KL, Vos PA, et al. Knee Images Digital Analysis (KIDA): a novel method to quantify individual radiographic features of knee osteoarthritis in detail. *Osteoarthritis Cartilage*. 2008;16:234–243.
139. van 't Klooster R, Hendriks EA, Watt I, et al. Automatic quantification of osteoarthritis in hand radiographs: validation of a new method to measure joint space width. *Osteoarthritis Cartilage*. 2008;16:18–25.
140. Goker B, Block JA. Improved precision in quantifying knee alignment angle. *Clin Orthop Relat Res*. 2007;458:145–149.
141. Lynch JA, Hawkes DJ, Buckland-Wright JC. Analysis of texture in macroradiographs of osteoarthritic knees using the fractal signature. *Phys Med Biol*. 1991;36:709–722.
142. Yamada K, Healey R, Amiel D, et al. Subchondral bone of the human knee joint in aging and osteoarthritis. *Osteoarthritis Cartilage*. 2002;10:360–369.
143. Langs G, Peloschek P, Bischof H, et al. Automatic quantification of joint space narrowing and erosions in rheumatoid arthritis. *IEEE Trans Med Imaging*. 2009;28:151–164.
144. Uebelhart D, Thonar EJ, Delmas PD, et al. Effects of oral chondroitin sulfate on the progression of knee osteoarthritis: a pilot study. *Osteoarthritis Cartilage*. 1998;6(Suppl A):39–46.
145. Oka H, Muraki S, Akune T, et al. Fully automatic quantification of knee osteoarthritis severity on plain radiographs. *Osteoarthritis Cartilage*. 2008;16:1300–1306.
146. Pfeil A, Bottcher J, Seidl BE, et al. Computer-aided joint space analysis (CAJSA) of the proximal-interphalangeal joint-normative age-related and gender specific data. *Acad Radiol*. 2007;14:594–602.
147. Mazzuca SA, Brandt KD, Buckland-Wright JC, et al. Field test of the reproducibility of automated measurements of medial tibiofemoral joint space width derived from standardized knee radiographs. *J Rheumatol*. 1999;26:1359–1365.
148. Baka N, de Bruijne M, van Walsum T, et al. Statistical shape model-based femur kinematics from biplane fluoroscopy. *IEEE Trans Med Imaging*. 2012;31: 1573–1583.
149. Barnabe C, Szabo E, Martin L, et al. Quantification of small joint space width, periarticular bone microstructure and erosions using high-resolution peripheral quantitative computed tomography in rheumatoid arthritis. *Clin Exp Rheumatol*. 2013;31:243–250.
150. Muhit AA, Arora S, Ogawa M, et al. Peripheral quantitative CT (pQCT) using a dedicated extremity cone-beam CT scanner. *Proc Soc Photo Opt Instrum Eng*. 2013;8672:867203.
151. Deschenes S, Charron G, Beaudoin G, et al. Diagnostic imaging of spinal deformities: reducing patients radiation dose with a new slot-scanning X-ray imager. *Spine (Phila Pa 1976)*. 2010;35:989–994.

152. Jorn LP, Friden T, Ryd L, et al. Persistent stability 3 years after reconstruction of the anterior cruciate ligament. A radiostereometric analysis (RSA) of 20 patients. *Acta Orthop Scand*. 1997;68:427–429.
153. Teeter MG, Leitch KM, Pape D, et al. Radiostereometric analysis of early anatomical changes following medial opening wedge high tibial osteotomy. *Knee*. 2015;22:41–46.
154. Dietrich TJ, Peterson CK, Brunner F, et al. Imaging-guided subacromial therapeutic injections: prospective study comparing abnormalities on conventional radiography with patient outcomes. *AJR Am J Roentgenol*. 2013;201:865–871.
155. Delin C, Silvera S, Bassinet C, et al. Ionizing radiation doses during lower limb torsion and anteversion measurements by EOS stereoradiography and computed tomography. *Eur J Radiol*. 2014;83:371–377.
156. Guggenberger R, Pfirrmann CW, Koch PP, et al. Assessment of lower limb length and alignment by biplanar linear radiography: comparison with supine CT and upright full-length radiography. *AJR Am J Roentgenol*. 2014;202: W161–W167.
157. Assi A, Chaibi Y, Presedo A, et al. Three-dimensional reconstructions for asymptomatic and cerebral palsy children's lower limbs using a biplanar X-ray system: a feasibility study. *Eur J Radiol*. 2013;82:2359–2364.
158. Gheno R, Nectoux E, Herbaux B, et al. Three-dimensional measurements of the lower extremity in children and adolescents using a low-dose biplanar X-ray device. *Eur Radiol*. 2012;22:765–771.
159. Buck FM, Guggenberger R, Koch PP, et al. Femoral and tibial torsion measurements with 3D models based on low-dose biplanar radiographs in comparison with standard CT measurements. *AJR Am J Roentgenol*. 2012;199: W607–W612.
160. Folinais D, Thelen P, Delin C, et al. Measuring femoral and rotational alignment: EOS system versus computed tomography. *Orthop Traumatol Surg Res*. 2013; 99:509–516.
161. Gaumetou E, Quijano S, Ilharreborde B, et al. EOS analysis of lower extremity segmental torsion in children and young adults. *Orthop Traumatol Surg Res*. 2014;100:147–151.
162. Rosskopf AB, Ramseier LE, Sutter R, et al. Femoral and tibial torsion measurement in children and adolescents: comparison of 3D models based on low-dose biplanar radiography and low-dose CT. *AJR Am J Roentgenol*. 2014;202: W285–W291.
163. Ilharreborde B, Steffen JS, Nectoux E, et al. Angle measurement reproducibility using EOS three-dimensional reconstructions in adolescent idiopathic scoliosis treated by posterior instrumentation. *Spine (Phila Pa 1976)*. 2011;36: E1306–E1313.
164. Glaser DA, Doan J, Newton PO. Comparison of 3-dimensional spinal reconstruction accuracy: biplanar radiographs with EOS versus computed tomography. *Spine (Phila Pa 1976)*. 2012;37:1391–1397.
165. Chhabra A, Thawait GK, Soldatos T, et al. High-resolution 3 T MR neurography of the brachial plexus and its branches, with emphasis on 3D imaging. *AJNR Am J Neuroradiol*. 2013;34:486–497.
166. Andreisek G, Crook DW, Burg D, et al. Peripheral neuropathies of the median, radial, and ulnar nerves: MR imaging features. *Radiographics*. 2006;26: 1267–1287.
167. Soldatos T, Andreisek G, Thawait GK, et al. High-resolution 3-T MR neurography of the lumbosacral plexus. *Radiographics*. 2013;33:967–987.
168. Pham M, Baumer T, Bendszus M. Peripheral nerves and plexus: imaging by MR-neurography and high-resolution ultrasound. *Curr Opin Neurol*. 2014;27: 370–379.
169. Chhabra A, Subhawong TK, Bizzell C, et al. 3 T MR neurography using three-dimensional diffusion-weighted PSIF: technical issues and advantages. *Skeletal Radiol*. 2011;40:1355–1360.
170. Kasper JM, Wadhwa V, Scott KM, et al. SHINKEI-a novel 3D isotropic MR neurography technique: technical advantages over 3DIRTSE-based imaging. *Eur Radiol*. 2015. [Epub ahead of print].
171. Eppenberger P, Andreisek G, Chhabra A. Magnetic resonance neurography: diffusion tensor imaging and future directions. *Neuroimaging Clin N Am*. 2014;24: 245–256.
172. Guggenberger R, Eppenberger P, Markovic D, et al. MR neurography of the median nerve at 3.0 T: optimization of diffusion tensor imaging and fiber tractography. *Eur J Radiol*. 2012;81:e775–e782.
173. Guggenberger R, Markovic D, Eppenberger P, et al. Assessment of median nerve with MR neurography by using diffusion-tensor imaging: normative and pathologic diffusion values. *Radiology*. 2012;265:194–203.
174. Setsompop K, Gagoski BA, Polimeni JR, et al. Blipped-controlled aliasing in parallel imaging for simultaneous multislice echo planar imaging with reduced g-factor penalty. *Magn Reson Med*. 2012;67:1210–1224.
175. Chabbra A, Andreisek G. *Magnetic Resonance Neurography*. London: Jaypee, 2012.
176. Chhabra A. Peripheral MR neurography: approach to interpretation. *Neuroimaging Clin N Am*. 2014;24:79–89.
177. Chhabra A, Ahlawat S, Belzberg A, et al. Peripheral nerve injury grading simplified on MR neurography: as referenced to Seddon and Sunderland classifications. *Indian J Radiol Imaging*. 2014;24:217–224.
178. Lustig M, Donoho D, Pauly JM. Sparse MRI: the application of compressed sensing for rapid MR imaging. *Magn Reson Med*. 2007;58:1182–1195.
179. Ma D, Gulani V, Seiberlich N, et al. Magnetic resonance fingerprinting. *Nature*. 2013;495:187–192.
180. Gao Y, Chen Y, Ma D, et al. Preclinical MR fingerprinting (MRF) at 7 T: effective quantitative imaging for rodent disease models. *NMR Biomed*. 2015;28: 384–394.
181. Chandra SS, Surowiec R, Ho C, et al. Automated analysis of hip joint cartilage combining MR T2 and three-dimensional fast-spin-echo images. *Magn Reson Med*. 2015. [Epub ahead of print].
182. Kruithof CJ, Kooijman MN, van Duijn CM, et al. The Generation R Study: Biobank update 2015. *Eur J Epidemiol*. 2014;29:911–927.